ANNUAL REVIEWS

Annual Review of Nuclear and Particle Science

The *Fermi*–LAT Galactic Center Excess: Evidence of Annihilating Dark Matter?

Simona Murgia

Department of Physics and Astronomy, University of California, Irvine, California 92697, USA; email: smurgia@uci.edu

Annu. Rev. Nucl. Part. Sci. 2020. 70:455–83

The *Annual Review of Nuclear and Particle Science* is online at nucl.annualreviews.org

https://doi.org/10.1146/annurev-nucl-101916-123029

Keywords

dark matter, indirect detection, Galactic center, γ-ray, excess

Abstract

The center of the Galaxy is one of the prime targets in the search for a signal of annihilating (or decaying) dark matter. If such a signal were to be detected, it would shed light on one of the biggest mysteries in physics today: What is dark matter? Fundamental properties of the particle nature of dark matter, such as its mass, annihilation cross section, and annihilation final states, could be measured for the first time. Several experiments have searched for such a signal, and some have measured excesses that are compatible with it. A long-standing and compelling excess is observed in γ-rays by the *Fermi* Large Area Telescope (*Fermi*–LAT). This excess is consistent with a dark matter particle with a mass of approximately 50 (up to ∼200) GeV annihilating with a velocity-averaged cross section of $\sim 10^{-26}$ cm^3 s^{-1}. Although a dark matter origin of the excess remains viable, other interpretations are possible. In particular, there is some evidence that the excess is produced by a population of unresolved point sources of γ-rays—for example, millisecond pulsars. In this article, I review the current status of the observation of the *Fermi*–LAT Galactic center excess, the possible interpretations of the excess, the evidence and counterevidence for each, and the prospects for resolving its origin with future measurements.

Contents

1. INTRODUCTION

Observational evidence for dark matter (DM) is overwhelming and imprinted at different scales—from rotational curves of galaxies to the dynamics of galaxies in galaxy clusters—and in the history and evolution of the Universe with cosmological observations of structure formation (1). In this context, one prominent question emerges: What is DM? Several theoretical scenarios have been proposed that predict the existence of a particle (or particles) whose properties explain the observations. This vast theoretical landscape includes DM candidates with masses that range from very light (a fraction of the mass of the electron) to heavier ones (hundreds of times the mass of the proton) and up to primordial black holes (2). Weakly interacting massive particles (WIMPs) fall within this broad range of possibilities, and their existence naturally arises in theoretical scenarios to complete them. A concerted effort to find experimental evidence for WIMPs and determine their properties is ongoing, and it relies on a three-pronged approach: collider, direct detection, and indirect detection (3). These searches have explored and ruled out large swaths of the parameter space for WIMP models and, in some cases, strongly challenge some of the frameworks. Intriguing signals have also been claimed. A notable example is the excess in γ-rays observed by the *Fermi* Large Area Telescope (*Fermi*–LAT) toward the center of the Milky Way, where a DM annihilation signal is predicted to be brightest. The spatial morphology, spectrum, and intensity of the excess are found to be compatible with a cold DM scenario in which the DM particle is a WIMP. The leading competing hypothesis to explain it is a population of discrete γ-ray emitters, millisecond pulsars (MSPs) in particular. Almost 10 years after the excess was discovered, and after many attempts to confirm it or rule it out, the signal and its DM interpretation remain viable. This review discusses the status of the observation (Section 2), the challenges in determining its properties (Section 3), its interpretation (Section 4), and prospects for settling its origin (Section 5).

2. THE GALACTIC CENTER IN γ-RAYS

An excess in the *Fermi*–LAT data in the direction of the Galactic center (GC) was first claimed in Reference 4. Several analyses since then have confirmed the presence of the excess (e.g., 5–13). The excess emission appears as an additional component in the γ-ray sky, with spectrum and spatial

morphology distinct from the other known astrophysical components, and properties generally consistent across different analyses.[1]

The GC excess is a subdominant component of the total γ-ray flux from the direction of the GC. In a region covering ∼2 kpc across at the GC, ∼90–95% of the γ-ray flux above 1 GeV is the result of cosmic ray (CR) interactions with the interstellar medium (see Section 3 for details). I refer to this dominant component as the interstellar emission (IE) or the interstellar emission model (IEM). The morphology of the IE is not simple or smooth; it depends on the distribution of CR sources, CR propagation, and the distribution of the interstellar medium. The model chosen for the IE thus significantly affects the characterization of the inferred properties of the GC excess—its spatial morphology and energy spectrum. For this reason, this review gives significant attention to the modeling of the IE. It is important to keep in mind throughout this discussion that different properties of the GC excess are possible within the uncertainties of the IE models that have been considered, and these variations correspond to different interpretations of the excess.

Various possibilities for the IEM have been considered, but they do not encompass the full extent of possible models (see Section 3). Assumptions and approximations apply to all IEMs employed, and, crucially, some of these assumptions are common to all analyses of the GC excess. It might be tempting to rule out some of the GC spectra and morphologies on the basis of data–model agreement considerations and restrict the allowed range to the IEMs that yield the best one. However, none of the IEMs employed so far provides a good description of the data (to the level of Poisson noise). For these reasons, it is premature to rule out possibilities at this stage, even those outside the current bounds.

This section provides an overview of the properties of the GC excess spectrum and spatial morphology as they have been determined so far. The breadth of possibilities for the spectrum and spatial morphology of the GC excess can be traced back to modeling of the IE. Caveats related to the IEM that affect the characterization of the GC excess are discussed in Section 3.

2.1. Spectrum

The prominent feature that characterizes the GC excess is a spectrum that peaks at a few GeV in energy, as shown in **Figure 1** for a representative set of analyses. These results illustrate the extent of the spectral variations determined so far (although some deviations from this picture are also possible, as discussed later in this section), assuming a spatial morphology for the GC excess that is consistent with DM annihilation (see Section 2.2 for a discussion of the spatial morphology).

The spectrum has a flux that is largest in the energy range of ∼1–3 GeV. This feature is generally consistent across analyses and, arguably, is a reliable hallmark of the GC excess. However, at higher energies (above ∼10 GeV), the presence of the GC excess is uncertain. This uncertainty is evident from the broad range of spectra above this energy displayed in **Figure 1**. Whether the spectrum includes a harder component above ∼10 GeV (extending up to ∼100 GeV) or cuts off at ∼10 GeV hinges on the IEM assumptions and analysis methodology. Because the GC excess is strongly correlated with other components of the IE, the high-energy component is attributed to the IE or to the GC excess, depending on the assumptions that are made. The dependence of the GC excess high-energy component on the IEM, and implications for its interpretation, are discussed more at length in Sections 3 and 4, respectively. Notably, the spectrum at high energy is an

[1]Another well-known excess in γ-rays in the GeV energy range is the one observed by the EGRET experiment (14), a precursor to *Fermi*–LAT. Unlike the *Fermi*–LAT GC excess discussed in this review, the EGRET GeV excess was observed in all directions of the sky, and it has not been confirmed by *Fermi*–LAT (15).

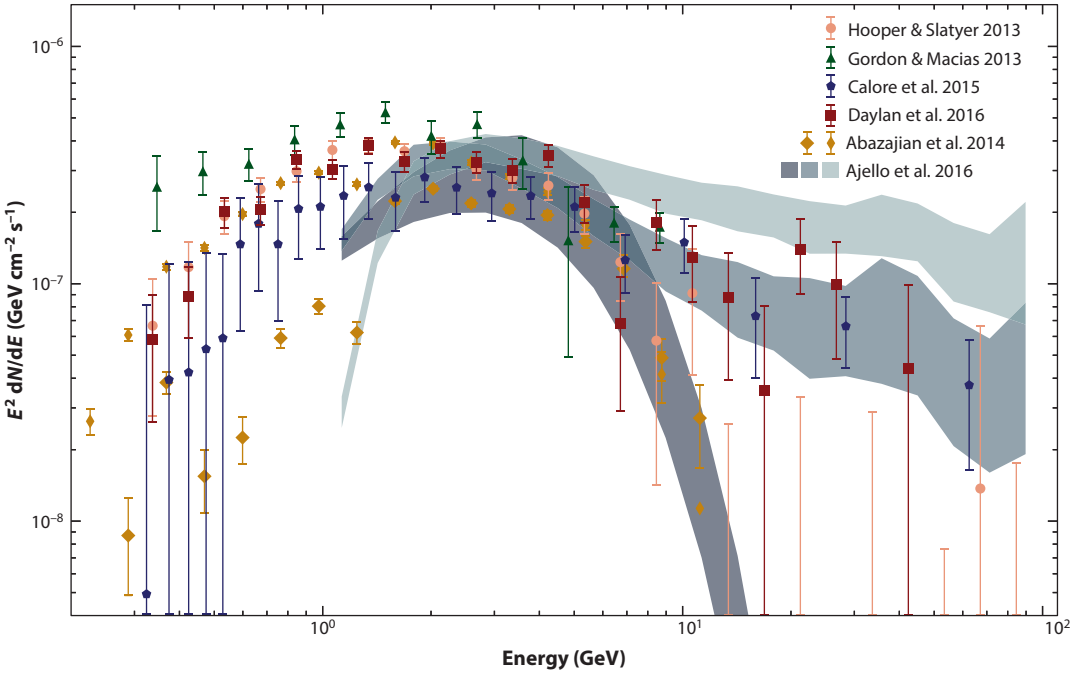

Figure 1

GC excess differential flux for a 15° × 15° region about the GC. Data from Hooper & Slatyer (8), Gordon & Macias (9), Abazajian et al. (10), Daylan et al. (11), Calore et al (12), and Ajello et al. (13). Because the analyses of the GC excess shown in this figure are based on regions of the γ-ray sky of differing sizes, for a direct comparison they have been rescaled to the dark matter content over the 15° × 15° region for a Navarro–Frenk–White profile with index $\gamma = 1$. Abbreviation: GC, Galactic center.

important discriminating factor between a DM or MSP interpretation of the excess. The lower-energy component of the GC excess spectrum, below ∼1 GeV, is also uncertain and covers large variations across analyses. Similar to the high-energy component, whether the spectrum steeply falls below this energy or not is crucial in identifying the origin of the GC excess, as discussed in Section 4.

Although the peak energy is generally accepted as a robust feature of the GC excess spectrum, it has been observed that, for a subset of IEM assumptions and parameterization of the GC excess spectrum, it can shift upward by a few GeV to about 5 GeV (e.g., 13). These results, which are not shown in **Figure 1**, do not yield as good an agreement with the data as those included in the figure. However, because of the uncertainties in the IE modeling, they cannot be conclusively ruled out at this time (see Section 3 for a discussion).

It also has been argued that the GC excess spectrum is not uniform across the region where it is detected but, rather, displays a spatial variation. Specifically, the spectrum might be harder in regions farther from the Galactic plane (16, 17) (see also Section 2.2). Implications of this spatial variation for the interpretation of the GC excess are presented in Section 4.2.1.

These results are an illustration of the variations in the GC excess spectrum when a DM spatial morphology that is spherically symmetric is assumed. Variations in the spatial morphology of the GC excess have been observed and are discussed in Section 2.2. In the context of the spectrum, it has been observed that when a spatial morphology for the GC excess that follows the Galactic stellar bulge is considered instead of DM, the flux is somewhat lower in the GeV range compared with other results but is otherwise compatible (18).

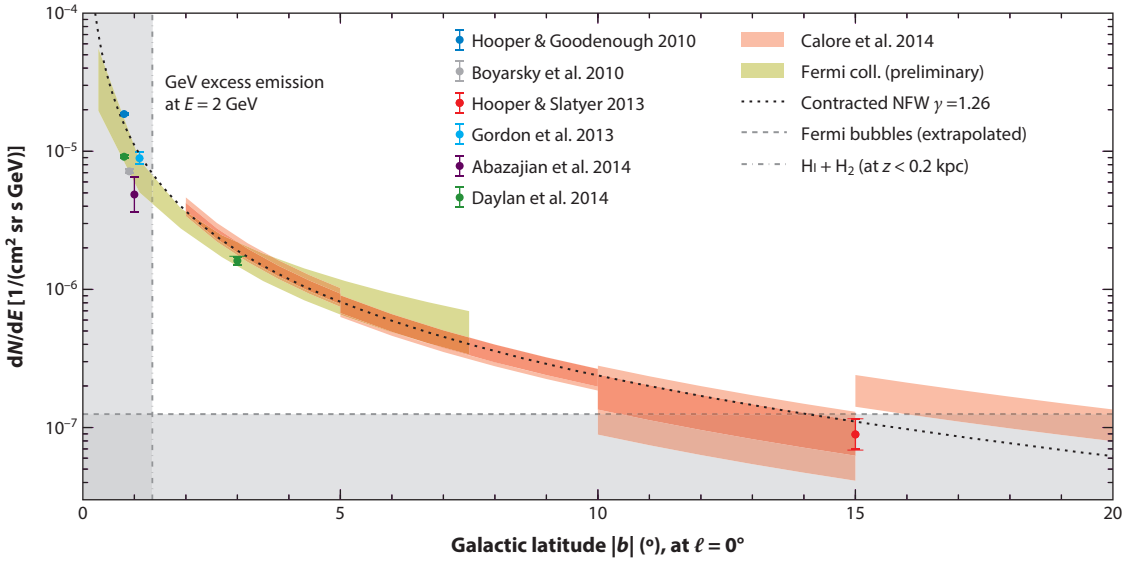

Figure 2

GC excess intensity at 2 GeV as a function of Galactic latitude from various studies (4, 8–12, 19). The result labeled "Fermi coll. (preliminary)" corresponds to Reference 13. The horizontal gray band indicates the (uniform) intensity of the Fermi bubbles (20; see also Section 3.2.5), extrapolated from latitudes above 10°, while the vertical gray band approximately delimits the region where the gas-related γ-ray emission from the inner Galaxy is significant. Abbreviations: GC, Galactic center; NFW, Navarro–Frenk–White. Figure adapted with permission from Reference 21.

2.2. Spatial Morphology

The spatial distribution of the GC excess is generally found to be consistent with a spherical morphology, which is brightest toward the GC. The dependence of the intensity on radial distance from the GC is shown in **Figure 2**. While most analyses exclude the data 1–2° from the GC, others (e.g., 13, 18, 22) include the innermost region. This distribution is consistent with an emission originating from DM annihilation for a Navarro–Frenk–White (NFW) (23) density distribution—that is, the γ-rays have a spatial morphology that is consistent with the square of the NFW distribution. The following parameterization for a generalized NFW profile is employed:

$$\rho(r) = \rho_0 \left(\frac{r}{R_s}\right)^{-\gamma} \left(1 + \frac{r}{R_s}\right)^{\gamma-3}, \qquad 1.$$

where γ is the slope of the DM distribution in the innermost region, and, in the context of the GC excess, its value is constrained by the γ-ray observation of the excess itself.[2] As for the other parameters, commonly assumed values are $R_s = 20$ kpc and ρ_0 corresponding to a local DM density in the range $\rho_\odot = 0.3$–0.4 GeV cm^{-3}. A profile in the range $\gamma = 1.1$–1.3 is favored by most analyses of the GC excess, but a shallower profile with $\gamma = 1$ is also allowed. The NFW profile with $\gamma = 1$ is predicted by simulations of cold DM, and a steeper distribution, with $\gamma > 1$, can arise when baryonic effects are included (25). The excess extends to approximately 10–15° from the Galactic plane (encompassing a distance of ∼1.5–2.3 kpc from the GC) (11, 12), and the centroid of the

[2]Measurements of the Milky Way stellar kinematics do not accurately constrain the NFW inner slope γ (e.g., 24).

distribution is found to be consistent with the position of the GC—more specifically, within 0.05° of Sgr A* (11). This broad-brush characterization of the GC morphology persists across numerous analyses; however, departures from it have been claimed.

The centroid of the GC excess might be offset from the GC by as much as ∼1° (12, 26, 27). Furthermore, the low-energy (below ∼10 GeV) and high-energy (above ∼10 GeV) components might correspond to different spatial morphologies: The high-energy tail might cut off in the innermost few degrees (17) (as discussed in Section 2.1), and the centroid offset might be larger at higher energies (12). If confirmed, these features would suggest that high- and low-energy components of the GC excess correspond to different underlying physical processes. Other studies, however, conclude that the high-energy and low-energy components favor the same radial profile (26, 27). It is also possible that the GC excess vanishes altogether above 10 GeV (as discussed in Section 2.1), and its properties in this energy range are correspondingly uncertain. Finally, deviations from a spherically symmetric morphology have been suggested, and the emission is found to be compatible with the stellar distribution in the Galactic bulge, which is boxy or X-shaped (18, 28, 29). This morphology would suggest that the GC excess emission originates from the stellar population in the Galactic bulge. However, a morphology that broadly traces the distribution of molecular gas in the inner Galaxy, a tracer of star-forming regions, is disfavored compared with a spherically symmetric distribution (13).

Studies of the spatial morphology of the GC excess rely on a selected set of spatial templates. These are generally well motivated but also, by nature, model dependent and limited. Consequently, other possibilities for the spatial morphology of the GC excess cannot be excluded at present.

3. MODELING THE INNER GALAXY

The γ-ray IE from the Milky Way is generated by CRs interacting with the interstellar medium (gas and radiation field). Growing evidence supports supernova remnants (SNRs) as the source of Galactic CRs (e.g., 30), which, as they propagate through the Galaxy, interact with the interstellar medium and produce the bulk of the Galactic γ-ray emission observed by *Fermi*–LAT. The following physical processes contribute to this emission: inverse Compton scattering of CR electrons on the interstellar radiation field (ISRF, covering optical, infrared, and CMB bands), gas-related interactions—that is, bremsstrahlung of CR electrons with the gas [atomic (HI), molecular (H_2), and ionized (HII) hydrogen]—and π^0 production from CR protons interacting with the gas. Models of the γ-ray emission from each of these processes rely on knowledge of the distribution of the target medium (gas, ISRF) and of the CRs in the Galaxy. The distribution of CRs depends on the distribution of CR sources, on the injection spectrum of CRs in the interstellar medium, and on propagation through the Galaxy. The region toward the GC is especially challenging to model: The line of sight includes the GC itself where the distribution of the interstellar medium and CR density is not well constrained, and it is also the longest across the Galaxy probing different Galactic environments (the fore/background contribution along the line of sight), including the local one, which also must be incorporated in the analysis of the GC region. The fore/background contribution is the largest fraction of the total emission toward the GC (e.g., ∼80% of the γ-rays in a 15° × 15° region, and energies above 1 GeV, are produced in interactions farther than ∼1 kpc from the GC) (13), and a careful assessment of the uncertainties in modeling it is crucial for the analysis of the GC region.

Many point sources also contribute to the observed emission toward the GC and can overlap along the line of sight. The uncertainty in the IE is closely intertwined with the ability to determine the point sources in this region as they can be difficult to disentangle from it. There is evidence that

some of the γ-ray point sources in the inner few degrees detected by *Fermi*–LAT trace structure in the gas rather than point-like sources such as pulsars, and this determination is strongly dependent on the assumptions of the IEM (13). Because of this dependence, point sources must be determined self-consistently with the IEM. A self-consistent determination of point sources and IEM in the inner Galaxy is employed by some studies of the GC excess (13); however, most analyses rely on existing *Fermi*–LAT point source catalogs derived with different assumptions on the IEM than those employed in the specific study. Disentangling true point source emission from structure in the IE is an important aspect of the analysis of the GC region and of the interpretation of the GC excess, as discussed in Section 4.3.

The discovery of the GC excess, and the possibility that it might be the first direct glimpse of the nature of DM, is tantalizing. A more accurate characterization of its spectrum and morphology is critical to resolve its origin. IE modeling uncertainties are the main challenge in achieving this goal. The GC excess is a relatively small fraction of the total emission over the line of sight toward the GC. As an illustration, for a $15° \times 15°$ region, and above 1 GeV, the GC excess accounts for ~5–10% of the line-of-sight emission toward the GC (13) (this fraction varies depending on the energy range and region of the sky considered, on the parameters that specify the DM density distribution, and on the IEM employed for the measurement of the excess). Although this fraction corresponds to thousands of signal events and a correspondingly large statistical significance, uncertainties of the IEM can be larger than the full size of the claimed signal. This section outlines the approaches employed to model this emission and describes some related challenges.

3.1. Approaches in Building the Interstellar Emission Model

Broadly speaking, the approaches employed in building the IEMs for the analysis of the GC excess are either empirically driven via template fits to the γ-ray data or rely on a priori knowledge of astrophysical inputs and CR propagation. Both approaches are rooted in assumptions, some of which are in common, for the production and propagation of CRs and for the distribution of the target medium. Regardless of the adopted methodology and assumptions, the GC excess is detected with high statistical significance. In practice, many analyses of the GC region are hybrid versions that attempt to exploit the advantages of both approaches; they are classified in this section based on how heavily they rely on each approach.

3.1.1. Template-based approach. This approach is based on templates that act as tracers for the Galactic γ-ray emission and that are tuned to the γ-ray data to determine properties such as the γ-ray emissivity of the gas and to extract other physical properties (e.g., radial dependence of the density of CR protons, and their spectrum) (31). The IEM is a linear combination of templates, which are gas related and inverse Compton modeled separately, with overall normalizations (or, for some of the analyses/templates, independently in energy bins) constrained by a fit to the data. The IEMs provided by the Fermi Science Support Center follow this approach (31; see also **https://fermi.gsfc.nasa.gov/ssc/data/access/lat/BackgroundModels.html**). The methodology is designed to flatten the data–model residual, and to help achieve such flattening, the models include patches for extended sources for which templates are not available to trace their emission. For this reason, these models are generally indicated for the study of sources with limited extension—that is, less than a few degrees. There is a delicate balance with the template method between introducing enough components to model the γ-ray IE (in agreement with the data) and introducing templates that cause the GC excess to be fitted away. This method is therefore not well suited for the study of the GC excess. Later versions of these models are maximally unsuited because some of the patches are designed to absorb the GC excess itself. Earlier versions of

these IEMs (e.g., P6_V11_DIFFUSE, available at **https://fermi.gsfc.nasa.gov/ssc/data/access/lat/BackgroundModels.html**) are used for the analysis of the GC excess because, although they include patches, these patches are not optimized to incorporate the excess. Despite the shortcomings, this approach is frequently used in the analysis of the GC excess.

Analyses that rely on this approach include those reported in References 7–9 and 11. The models included in these analyses have in some cases been refined by incorporating improved templates for some of the model components. For example, improved templates based on hydrodynamical simulations are added to the models for a more realistic representation of the kinematics of the Galactic central bar (18, 28). In addition, alternative fitting techniques are employed in which nuisance parameters are included in the fit to accommodate small variations at the pixel-by-pixel level to ultimately account for uncertainties in the spatial distribution of some of the templates (29). The spatial morphology of the GC excess is significantly affected by these choices and, in some cases, is found to be more compatible with the stellar population in the inner Galaxy compared with a spherical morphology (and a DM interpretation) (18, 28, 29).

3.1.2. Propagation code–based approach. An alternative approach in building the IEM is designed to predict the γ-ray IE based on assumptions regarding CR injection spectra, CR propagation, CR density distribution, and the distribution of the interstellar medium. Assumptions are based on a broad set of astrophysical inputs and are not tuned to the γ-ray data. This approach relies on a CR propagation code (GALPROP is widely used; see **https://galprop.stanford.edu**) to calculate the CR intensities across the Galaxy, in agreement with CR data at the solar system, and to fold them with the distribution of the interstellar medium to produce maps of the γ-ray emission. The input parameters for these models are many, and their values can have large uncertainties. Extensive studies have been performed to constrain parameters such as the CR source distribution, size of the CR confinement volume, and distribution of the interstellar gas, by creating a grid of possible parameter values to be used in the calculation of the maps, and to test their agreement with the γ-ray data from *Fermi*–LAT (32). These a priori models provide good agreement with the data across the sky, at the level of 10–20%; however, they do not fully capture the complexity of the Galaxy. Analyses for the GC excess that are based on this approach often adopt these a priori models as a baseline and incorporate template fitting to tune these models for the analyses of the GC region. Analyses that illustrate this methodology include those reported in References 12 and 13.

A range of variations in the distribution of CR sources, their injection spectrum, distribution of the interstellar medium, propagation, and magnetic fields has been employed in Reference 12. Extreme scenarios are also considered that are excluded by CR and γ-ray data in an attempt to more generously bracket the IEM uncertainties. The model components are tuned to the γ-ray data, and additional degrees of freedom are allowed by fitting the spectrum for some of the model components in independent energy bins. The GC excess spectrum depends on these assumptions (see **Figure 1**), although the variations considered in this study do not cover the full extent of the observed spectrum.

These analyses of the GC excess generally determine the contribution of the fore/background emission to the GC region by fits to all-sky γ-ray data, which include the GC region itself. In Reference 13, this component is instead judiciously tuned to selected regions that exclude the bulk of the GC excess and other emissions associated with the GC (e.g., the Fermi bubbles; see Section 3.2.5). This methodology is therefore less susceptible to biases that these components might introduce in the determination of the GC excess. Regions at least 1 kpc away from the GC are used to constrain the fore/background contribution, and this contribution is held fixed when analyzing the data toward the GC. Because of the independent tuning of the fore/background, this

methodology is designed to also extract the γ-ray emission from the inner 1 kpc by separating it from the rest of the line of sight and to independently tune it to the data. A wider range of spectra for the GC excess is found by this analysis (see **Figure 1**), encompassing a broad range of the observed spectral variation of the GC excess, with a set of well-motivated selected assumptions on the CR source distribution and their spectrum/propagation.

Both of the approaches described above have merits. The template-based approach is less sensitive to a priori assumptions (and related uncertainties) on CR production, propagation, and interaction, and it produces IEMs that better agree with the data. The propagation code IEMs are sensitive to the limits on the sophistication of the physics models that are considered; however, these IEMs are less susceptible to absorbing new, unmodeled extended signals in the data and are therefore preferable for the analysis of the GC excess. Both approaches are constrained by the validity of the assumptions that are made, built into the templates or in the input parameters (some of which are degenerate with each other). These assumptions do not encompass all possibilities, and many are common to all approaches and analyses. These difficulties and the implications for the GC excess are discussed in Section 3.2.

3.2. Limitations of the Interstellar Emission Models for the Galactic Center Excess Analysis

Limitations in building the IEMs and their impact on the characterization of the GC excess are reviewed in this section.

3.2.1. Cosmic ray source distribution near the Galactic center. IEMs rely on assumptions regarding the distribution of CR sources in the Galaxy and other properties, such as their injection spectrum. Because their spatial distribution is not well constrained, proxies such as pulsars or OB stars (corresponding to later and earlier stages in the life of the star) are commonly employed to model the distribution of CR sources. Observational biases in tracing these source populations result in large uncertainties that affect the inferred CR source distribution. As an illustration, these distributions all assume a paucity of sources within a few kiloparsecs from the GC, which might not be a realistic assumption. Because of the poorly constrained distribution of CR sources in the vicinity of the GC, it is possible that the GC excess is at least partially explained by additional CR sources on top of those previously assumed, and there is evidence to support this hypothesis. For example, an enhancement of the CR source population at the GC in the IEM would give rise to a brighter inverse Compton contribution. This possibility is compatible with the data: The measured *Fermi*–LAT γ-ray inverse Compton emission from within the inner $\sim$1 kpc is larger than that predicted by models with a paucity of CR sources near the GC. More CR sources (and/or higher-intensity ISRF) can plausibly explain the inverse Compton enhancement and account for a portion of the GC excess (13). Furthermore, incorporating additional CR sources in the model can significantly alter the properties of the GC excess. For example, an additional steady-state CR source component in the IEM that traces a spatial morphology compatible with the observation of the GC excess can account for most of its emission (33). Alternatively, injecting more CRs near the GC with a distribution tracing the density of collapsed H_2 molecular clouds reduces the excess and significantly modifies its properties (22, 34).

3.2.2. Distribution of the interstellar gas toward the Galactic center. The distribution of gas in the Galaxy is inferred from radio surveys. The line-of-sight velocity of the gas together with the rotation curve of the Galaxy uniquely specifies the radial distance of the gas from the GC, assuming circular motion of the gas. The resulting maps, split in Galactocentric annuli and

convoluted with the CR density distribution, serve as templates for the HI- and H_2-related γ-ray emission. However, for gas within about $\pm 10°$ in longitude from the GC, this procedure breaks down because the kinematic resolution deteriorates and there is no reliable way to split the gas according to Galactocentric distance. This issue can be addressed by interpolating the gas column density from larger angular distances. This procedure, described in Reference 32, leads to arbitrary placement of the gas along the line of sight and, together with the varying CR density, to likely mismodeling of the γ-ray emission in this direction. It has been estimated that this approximation yields a pixel-to-pixel variation as large as $\sim$15% of the emission (for a $15° \times 15°$ region centered at the GC) and presumably even larger closer to the GC because of the less reliable interpolation farther from the boundary of the interpolation region (13). The quoted uncertainty is only illustrative as it relies on other assumptions, but it demonstrates that significant spurious artifacts can be introduced in the residual emission based on misplacement of the gas. Hydrodynamical simulations have also been employed to separate the gas along the line of sight in the inner Galaxy, to model the noncircular motion induced by the Galactic bar (18).

The column density of H_2 in the Galaxy is probed not directly but, rather, via proxies—that is, using other molecules such as CO that are also present in H_2 clouds. A conversion factor is used to infer the H_2 content based on surveys of its proxies. There is evidence based on γ-ray observations that the conversion factor is not the same throughout the Galaxy and varies in different environments (32). Its value is not known a priori, and it contributes to the uncertainties in modeling the H_2-related γ-ray emission. Ajello et al. (13) have found evidence for an asymmetry about the GC for the positive residual emission, suggesting that the GC excess might indeed depart from the spherical symmetry that is generally claimed. However, the residual emission also shows mismodeling (deficits) that corresponds to features of the H_2-related γ-ray emission. It is therefore plausible that the H_2 column density has been mismodeled because of uncertainties in the conversion factor, generating a spurious asymmetry in an otherwise spherically symmetric underlying excess emission. Thus, caution is necessary in interpreting the structure in the GC excess emission because of the interplay with other structured γ-ray components.

3.2.3. Inverse Compton emission from the Galactic center region. As discussed in Section 3.2.1, there is strong evidence that the inverse Compton emission within $\sim$1 kpc of the GC is far brighter than predicted. This finding can be explained if this region encloses a higher density of CRs (see Section 3.2.1) and/or a higher intensity of the ISRF than previously assumed. This does not exclude that a more peaked distribution such as a DM annihilation component might also contribute to the data. Because of the strong correlation between these two components (inverse Compton and DM), their contributions are difficult to disentangle (12, 13). Furthermore, when the inverse Compton and gas-related γ-ray emission from the inner 1 kpc are split from the fore/background emission and fitted to the data, they are found to be anticorrelated. The corresponding spatial residuals are less structured compared with other analyses of the GC excess and compatible with a smoother spatial morphology. Better understanding of the inverse Compton emission in the GC region is therefore crucial to characterize the excess.

3.2.4. 3D modeling. The γ-ray IEMs used for the analysis of the GC excess have relied almost exclusively on 2D modeling of the interstellar gas, ISRF, and CR density distribution. Cylindrical symmetry is assumed. This assumption is not representative of the true, and more complex, structure of the Galaxy with its spiral arms and the Galactic bar and bulge. There is evidence of emission in the γ-ray data that can be traced back to these structures (13). An attempt to estimate the uncertainty related to assuming cylindrical symmetry is made in Reference 13, and this uncertainty can be $\sim$2% of the emission toward the GC from the entire line of sight for a

$15° \times 15°$ region (encompassing ~1 kpc at the distance of the GC). This is a significant fraction of the GC excess itself, which in this analysis accounts for ~5–10% of the line of sight toward the GC for the same region. More recently, models that incorporate a more realistic 3D structure for the Galaxy have been devised (e.g., 35, 36), and their predictions significantly differ from those of their 2D counterparts. In particular, 3D modeling of the ISRF and CR sources predicts features that explain structures in the *Fermi*–LAT data and that are related to the spiral arm structure not present in 2D models (35). These models can also plausibly explain the enhanced inverse Compton emission from the inner kiloparsecs found by Ajello et al. (13) with an additional CR bulge/bar source density distribution. These studies illustrate that the impact of 3D modeling is significant and cannot be neglected when interpreting extended residuals such as the GC excess.

An implementation of 3D modeling for the γ-ray inverse Compton component (from Reference 35) in the analysis of GC excess confirms its presence, with properties that fall within the current bounds (28). Complementary work employing 3D modeling for gas density (and, to some extent, particle diffusion), in addition to a revised CR source population that traces star-forming regions near the GC, has found that these assumptions also significantly alter the model predictions and the properties of the GC excess (34).

3.2.5. Fermi bubbles. The Fermi bubbles (20) are large γ-ray structures that extend approximately 50° above and below the Galactic plane. While this emission and the GC excess are not likely to share a common origin, their interplay in the modeling is significant (8, 26, 37) and presents an additional challenge in the analysis of the GC excess. For context, the (uniform) intensity of the Fermi bubbles is compared with the radial dependence of the GC excess in **Figure 2**. To limit the impact of the Fermi bubbles on the analysis of the GC excess, the high-latitude contribution of the Fermi bubbles can be excluded from the analysis (e.g., 37). Most analyses, however, include this component in the model based on a high-latitude determination, where the contribution of the Fermi bubbles is less challenging to model. At lower latitudes, it is difficult to disentangle the Fermi bubbles from the other γ-ray components. As a result, uncertainties in modeling their contribution in the region that overlaps most with the GC excess are large and can significantly reduce the intensity of the GC excess, to the extent that modeling the Fermi bubbles component in this region can cause the excess to vanish above 10 GeV (37). Recently proposed IEMs that deviate from the steady-state assumption and allow for time-dependent CR injection and propagation also affect the characterization of the Fermi bubbles, and incorporating these improved models in the analysis of the GC excess might also alter its properties (38).

3.2.6. Empirical uncertainties. A complementary attempt to assess IEM uncertainties has been spearheaded by Calore et al. (12). In addition to probing a vast theoretical parameter space for the modeling uncertainties, as described in Section 3.1, an empirical determination is also considered. This approach uses the residuals along the Galactic plane as an estimate of the IEM uncertainties. These discrepancies, which can be traced back to variations in the normalization and spectrum of the IEM components, constitute an empirically determined uncertainty on the GC spectrum. Its magnitude is comparable to the theoretical one found in this study, which is shown in **Figure 1**.

As discussed in the subsections above, progress has been made in addressing the shortcomings of the IEMs used in the analysis of the GC excess and in assessing the full scope of the uncertainties. Results based on these improvements do not, so far, question the existence of the GC excess, but they widen the range of possibilities for its properties—that is, intensity, spectrum, and spatial distribution. For example, whether the spatial morphology of the GC excess is spherical or X-shaped—which is a crucial issue in resolving the nature of the excess—strongly relies on the IE modeling near the Galactic plane, including the uncertain contribution of the Fermi bubbles,

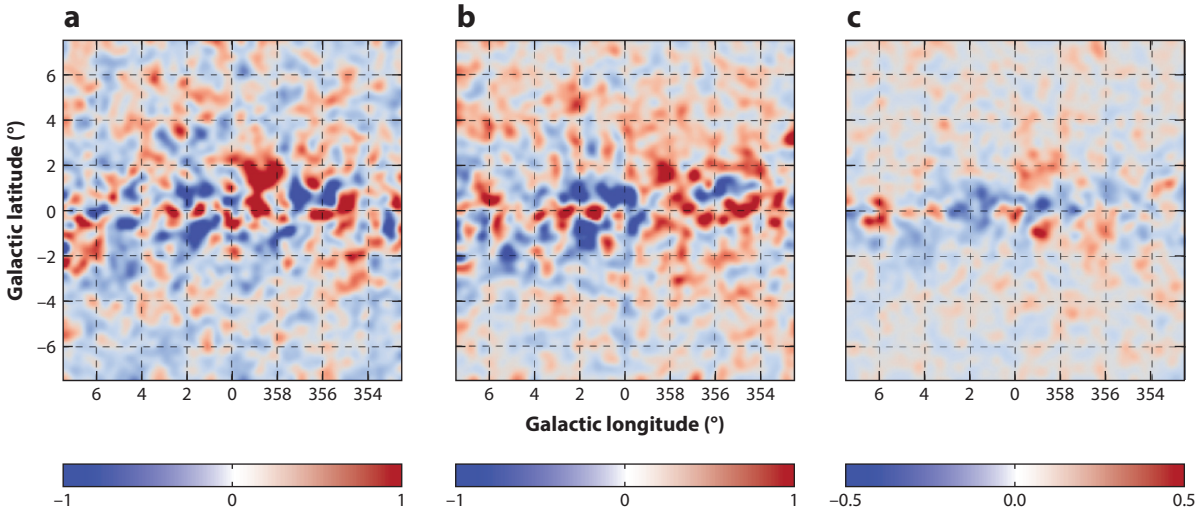

Figure 3

Residual counts (data–model) in three energy bands: (*a*) 1–1.6 GeV, (*b*) 1.6–10 GeV, and (*c*) 10–100 GeV. Figure adapted with permission from Reference 27.

where modeling these components is very challenging. Similarly, spectral properties can vary significantly and are sensitive to the assumptions and methodology employed.

To further understand the implications of the IEM uncertainties in the context of the GC excess, it is important to reiterate that agreement with the data at the level of statistical fluctuations is not achieved by any of these models. Excesses and deficits, which remain even after the GC excess has been accounted for, suggest shortcomings in the IEMs that have yet to be addressed. An example of the residual emission is shown in **Figure 3**, where the residuals (data–model) from Reference 27 are shown in three energy bands (the GC excess is included in the model with a DM spatial morphology). Because of the IEM limitations, interpretations of the GC excess that correspond to IEMs with poorer agreement with the data should not be readily ruled out because the discrepancies could be explained by yet-unaccounted-for uncertainties in the IEMs.

Further refinements of these models will undeniably help in constraining the properties of the GC excess more reliably. However, prospects to conclusively resolve the nature of the GC excess exclusively on the basis of these improvements are limited because of the complexity involved, as described in this section.

4. INTERPRETATION

Interpretations of the GC excess emission are discussed in this section. They are based on current estimates of the uncertainties of the GC excess spectrum, spatial morphology, and intensity. As such, the interpretations proposed so far might not be comprehensive. Furthermore, it is plausible that more than one phenomenon is at the origin of the observation.

4.1. Dark Matter

Because of the suggestive spatial morphology and a spectrum that can be effortlessly explained as a by-product of annihilating DM, a DM interpretation of the GC excess has been popular since the first claim of a discovery. On the basis of current results, the GC excess is compatible

with a cold DM scenario in which the DM is a WIMP. Within the current constraints, the spatial morphology is consistent with a DM annihilation spatial distribution.[3] The shape of the spectrum constrains the annihilation final state(s) and WIMP mass. The γ-ray intensity and spectrum from DM annihilation are determined by

$$\frac{\mathrm{d}N_\gamma}{\mathrm{d}E} = \sum_f \frac{\langle \sigma_f v \rangle}{4\pi\,\eta\,m_\chi^2} \frac{\mathrm{d}N_\gamma^f}{\mathrm{d}E} \times \int_{\Delta\Omega} \mathrm{d}\Omega \int_{\mathrm{los}} \mathrm{d}s\; \rho^2(\mathbf{r}(s,\mathbf{n})), \qquad 2.$$

where f is the annihilation final state, $\langle \sigma_f v \rangle$ is the annihilation cross section (averaged over the DM velocity profile), m_χ is the DM particle mass, and $\mathrm{d}N_\gamma^f/\mathrm{d}E$ is the number of γ-rays per annihilation channel and is summed over all of the annihilation channels, $\eta = 2(4)$ for Majorana (Dirac) DM. The inner integral is the $\mathcal{J}$-factor, which is the integral of the DM density $\rho^2(\vec{x})$ (from Equation 1) over the line of sight (los) in direction $\mathbf{n}$.

For IEMs in which the spectrum of the GC excess cuts off at ∼10 GeV, models with a DM particle of mass ∼30–60 GeV, annihilation cross section $\langle \sigma_f v \rangle \sim 1\text{–}5 \times 10^{-26}$ cm^3 s^{-1}, and annihilations into hadronic final states (mainly bottom quarks) are favored (6, 7, 9, 11, 12). This corresponds to the simplest sort of WIMP thermal relic model of DM. The space of possible models opens up considerably when a broader set of IEMs is considered. For IEMs based on propagation code models (see Section 3.1.2) and an extensive scan of CR propagation parameters, larger DM masses as high as $m_\chi \sim 74$ GeV for annihilations into bottom quarks are allowed, as well as annihilation into pairs of Higgs bosons produced nearly at rest for $m_\chi \sim 125$ GeV (21). Alternative IEMs that further increase the range of allowed spectra (13) widen the parameter space for the DM particle: Annihilations into pairs of electroweak gauge bosons, Higgs bosons, or top quark/antiquarks (WW, ZZ, HH, $t\bar{t}$) are possible for masses m_χ between the production threshold and up to 165 GeV (WW), 190 GeV (ZZ), 280 GeV (HH), and 310 GeV ($t\bar{t}$). Annihilations into $b\bar{b}$ also provide a good fit to the data, and the allowed mass range, which is wider than those found in other analyses, covers 35 GeV $< m_\chi <$ 165 GeV in DM mass (40).

The γ-ray signal from DM might also include secondary inverse Compton and bremsstrahlung emission from e^-e^+ pairs produced in the annihilation process and interacting with the interstellar medium, thus altering the spectrum. For example, the bremsstrahlung contribution would soften the GC excess spectrum at lower energy and closer to the Galactic plane (11, 41, 42). Secondary inverse Compton emission might also play a role in distinguishing between different interpretations of the GC excess (see Section 4.2.1).

A DM interpretation of the GC excess can be constrained by independent experiments and observations. These constraints are discussed in the remainder of this section.

4.1.1. Constraining the dark matter interpretation with direct detection and collider searches. Constraints on the DM interpretation of the GC excess with direct detection and collider searches require a specific model because the associated cross sections are not directly related to the annihilation cross section. In this section, constraints are discussed in the context of the minimal supersymmetric extension of the Standard Model (MSSM), which is a prototypical model of WIMPs, and a few other models. Alternatively, constraints have also been derived in the framework of an effective field theory (EFT) by considering a general class of models with specified interactions for the DM particle dictated by symmetry arguments (e.g., local Lorentz

[3] As mentioned in Section 2.2, the centroid of the distribution might be offset with respect to the dynamical center of the Galaxy. It has been shown that such an offset is consistent with numerical DM simulations, with the largest offsets correlated with flatter central profiles (39), as discussed in Reference 27.

invariance, global quantum charges). An advantage of this framework is to readily evaluate the viability of the regions of the parameter space for indirect detection with constraints from direct detection and collider DM searches, which are also discussed in this section.

The GC excess is compatible with the MSSM if its spectrum extends above 10 GeV (40, 43–45). These results are consistent with a DM particle annihilating into several possible final states (bottom quarks, top quarks, or WW) and with a broad allowed range for its mass m_χ, spanning the interval ∼45–300 GeV. Large swaths of this parameter space are, however, ruled out by constraints from direct detection experiments. The excluded regions correspond to the low to intermediate mass ranges, while a neutralino with mass $m_\chi \sim 250$ GeV annihilating predominantly into top quarks survives. This interpretation is within the reach of future direct detection experiments that will confirm it or rule it out (45). In addition to the MSSM, the GC excess is consistent with DM candidates in Higgs portal models as well as with other simplified models (40).

While direct detection experiments have been instrumental in ruling out large areas of the parameter space, collider searches are not typically as constraining as direct detection experiments because they are generally more sensitive to lower-mass DM particles than those compatible with the GC excess. They can, however, constrain some simplified models in which tree-level diagrams for DM annihilation are considered that could explain the GC excess (46). Nevertheless, it is still an open possibility that the GC excess could be confirmed by collider experiments. A recent illustration of such a possibility is the potential excess in trilepton events observed by the ATLAS detector. This observation is claimed to be consistent with a lightest neutralino mass of approximately $m_\chi \simeq 60$ GeV in low-energy supersymmetric models and to be compatible with the GC excess (47). The predictions for this model are below the current reach of direct detection experiments.

Interpretations of the GC excess for an EFT have been determined. A general class of models has been considered in which the annihilation process is mediated by either pseudoscalar or vector interactions for quarks and leptons in the final states, and the coupling strength of these interactions is constrained via a fit to the data (27). The result is a DM particle with a mass in the range $m_\chi = 50$–190 (10–90) GeV and an annihilation cross section of approximately 1×10^{-26} to 4×10^{-25} (6×10^{-27} to 2×10^{-25}) cm^3 s^{-1} for pseudoscalar (vector) interactions. For pseudoscalar interactions, annihilations occur predominantly into bottom quarks for $m_\chi \sim 50$ GeV and into top quarks for higher masses ($m_\chi \sim 190$ GeV). Vector interactions cover a similar region in m_χ and $\langle \sigma_f v \rangle$, although lower masses ($m_\chi \sim 10$ GeV) are also allowed, for which annihilations occur primarily into leptonic final states. Comparably low masses and annihilations into leptons for the DM interpretation of the GC excess have also been found in previous work (e.g., 6). The viability of these regions in the parameter space can be compared to constraints from direct detection and collider DM searches. To this end, the GC excess–allowed intervals are mapped into the corresponding WIMP-nucleon scattering cross sections; the result is that models in which the annihilation is mediated by vector interactions are generally ruled out by the null results from direct detection experiments, for all but $m_\chi \sim 10$ GeV and for annihilations into leptons. Pseudoscalar models predict spin-dependent and velocity-dependent scattering with nuclei at a rate that is well below the current sensitivity but that in some cases is within the reach of future direct detection experiments [e.g., DARWIN (48) for the lower mass range]. As already mentioned, collider searches are typically not as competitive with direct detection for constraining the GC excess, and in the EFT scenario discussed here, such searches are more sensitive to models with light mediator particles.

4.1.2. Constraining the dark matter interpretation with astrophysical data. Other γ-ray DM targets are promising probes of a DM origin of the GC excess and are sensitive to scenarios

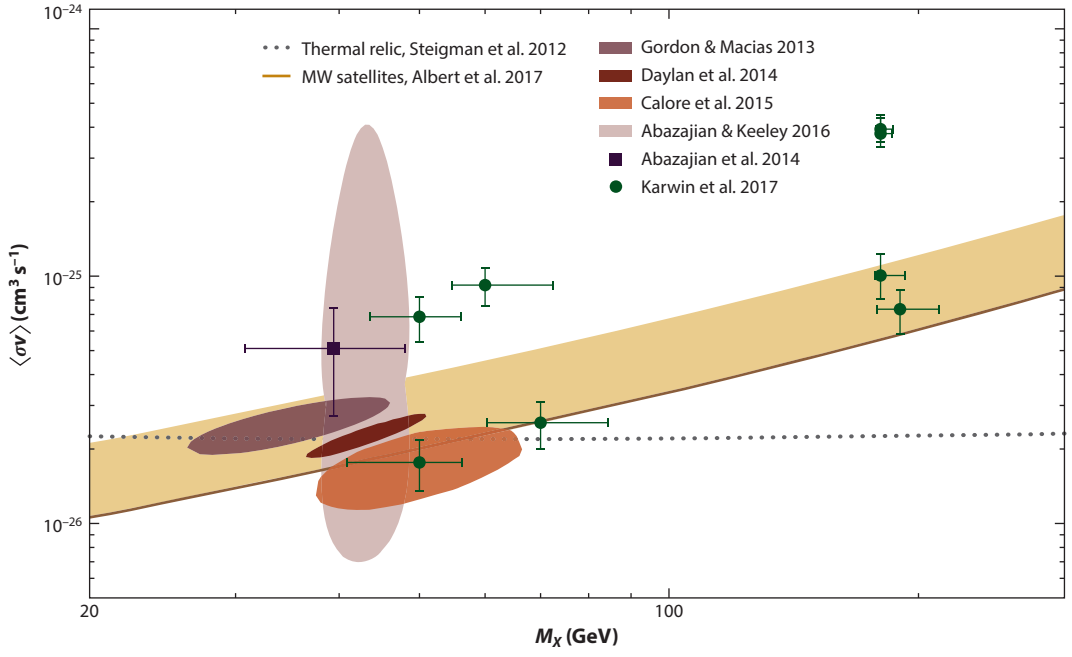

Figure 4

Regions of the parameter space compatible with a dark matter interpretation of the Galactic center excess (contours and points with error bars). Data from Gordon & Macias (9), Abazajian et al. (10), Daylan et al. (11), Calore et al. (12), Abazajian & Keeley (55), and Karwin et al. (27) (all corresponding to 2σ, except for References 10 and 55). These are compared with the thermal relic annihilation cross section (*gray dotted line*) (56) and with the constraints from dwarf spheroidal galaxies (*solid brown line*) (54). The tan band illustrates variations on the dwarf spheroidal constraints by a factor of two (57, 58) related to the assumptions for their dark matter halos, but larger variations that weaken the constraints up to a factor of seven are also possible (59). Abbreviation: MW, Milky Way.

that are out of reach for direct detection and collider searches. Although the center of the Galaxy is predicted to be the brightest for a DM annihilation signal, other targets might provide more reliable detections because they are less susceptible to the limitations in modeling of the IE (for a recent review, see 49; see also 50–52). Dwarf spheroidal galaxies belong to this category and are arguably the most promising targets for these searches. They are the largest DM clumps predicted by cold DM *N*-body simulations of galaxy formation. As they contain stars, they are observed optically. These systems are not expected to emit γ-rays through conventional astrophysical processes. In addition, the determination of the $\mathcal{J}$-factor for dwarf spheroidals is less dependent on the choice of the DM density profile because it is integrated over the entire volume of the dwarf spheroidal DM halo, unlike for the GC, where changes in slope can significantly alter the $\mathcal{J}$-factor. To date, there is no confirmed detection of dwarf spheroidal galaxies in γ-rays.[4] Constraints based on these observations have produced the most robust limits on the DM annihilation cross section to date. The most recent limits are shown by the solid brown line in **Figure 4**. Constraints have been determined for several possible annihilation final states, and those shown in **Figure 4** assume DM annihilating into bottom quarks (54).

[4]Tentative detections of dwarf spheroidal galaxies with *Fermi*–LAT have been claimed (53, 54); however, the detection is faint and is sensitive to the IEM.

The limits from dwarf spheroidals are overlaid with regions of the parameter space that are compatible with the DM interpretation of the GC excess. The allowed regions for the analyses of the GC excess are shown in **Figure 4** as contours with different shades or as circles/squares with error bars (indicating the allowed mass range and uncertainty on the cross section for the best-fit mass). Most of the allowed regions favor a DM particle mass in the range of ∼50 GeV, but higher values at around ∼200 GeV are also allowed. The illustrative set of results included in **Figure 4** has been chosen to display the broad range of masses that are compatible with the GC excess, but, as discussed in Section 4.1, intermediate values are also possible (in addition, the results from Reference 27 correspond to a discrete set of assumptions used to derive the IEMs, and other values that might allow intermediate mass and cross section regions not shown in **Figure 4** are not ruled out). If taken at face value, the results in **Figure 4** show that the dwarf spheroidal constraints rule out a fair fraction of the GC excess–allowed regions, especially at higher masses. This conclusion is unwarranted at present. Neither the GC excess contours nor the dwarf spheroidal constraints fully incorporate all the relevant uncertainties. Considerations on the determination of the $\mathcal{J}$-factor and the IEM affect these results and suggest that the range of masses and cross sections that are possible is broader than those shown in **Figure 4**, as discussed below.

The values of the Galactic DM density inner slope γ and the local DM density $\rho_\odot$ vary with analysis.[5] Steeper density profiles are generally considered (and are favored by the measurements). As for the local DM density, a value or range of values is chosen based on other constraints, and its uncertainty is discussed further in this section. Different values of γ and $\rho_\odot$ yield different $\mathcal{J}$-factors for the Galactic DM distribution, with larger values corresponding to lower annihilation cross sections for a measured γ-ray flux, and therefore induce shifts along the annihilation cross section axis. In addition to variations in the parameterization of the DM distribution, modeling of the IE affects these regions, shifting them diagonally and stretching out the allowed mass range. The results of Reference 27 include multiple final states in the fit to the data, and although they are consistent with annihilation largely into bottom quarks, they also allow for some fraction of the annihilations into leptonic final states. It should be noted that the allowed parameter space at higher masses corresponds to annihilations into top quarks, while the dwarf spheroidal constraints assume DM annihilations into bottom quarks and do not precisely apply.

The scatter of the contours in **Figure 4** illustrates that none of the GC excess DM interpretation results fully account for the known uncertainties in IE modeling and in the Galactic DM distribution. The allowed parameter space is indeed larger than any of these results indicate. The GC excess–allowed regions depend on uncertainties in the Galactic parameters of the NFW profile (55). It is possible that the range for the local DM density is broader ($\rho_\odot \approx 0.1$–0.5 GeV cm^{-3}), exceeding the values that have been considered in most analyses so far and correspondingly widening the allowed annihilation cross section range (55, 60). Dwarf spheroidal constraints are also affected by assumptions [e.g., on the morphology of the DM halo in these systems (61)] and can be weaker by a factor of two (this range is indicated by the tan-colored band in **Figure 4**) if their DM halos are not spherically symmetric (57, 58) and possibly by a factor as large as seven if more conservative priors are considered for the density profile (59). These considerations open up the range of possibilities for the GC excess, in particular for the higher DM particle masses

[5]These contours correspond to different values of the local DM density, which is $\rho_\odot = 0.4$ GeV cm^{-3} for most results included in **Figure 4** (11, 12, 27) except for those from Reference 10, where $\rho_\odot = 0.3$ GeV cm^{-3} is used, and Reference 55, where a range of data-driven values is explored, $\rho_\odot = (0.28 \pm 0.08)$ to (0.49 ± 0.13) GeV cm^{-3}. The slope for the inner DM density profile is $\gamma = 1.2$ for References 11, 12, and 27, while gentler profiles ($\gamma = 1$–1.1) are considered in References 27 and 55.

(∼200 GeV) shown in **Figure 4**. Dwarf spheroidal observations therefore cannot currently distinguish between a scenario in which the GC DM interpretation is comfortably allowed and one in which it is completely ruled out.

In addition to the GC and dwarf spheroidals, a promising DM target in γ-rays is the Andromeda galaxy (62). Its DM halo extends several degrees across the sky (∼40° for a DM halo 600 kpc across). *Fermi*–LAT found evidence of a spherical γ-ray halo around Andromeda, ∼1° across and fully correlated with tracers of γ-rays—that is, regions rich in gas or star formation activity (63, 64). This emission is compatible with the DM interpretation of the GC excess, but it can also originate from pulsars (65, 66). Neither DM nor pulsars are likely to account for most of the emission, but each might explain a fraction of it. Although this signal is intriguing, overlapping contributions make disentangling a potential DM signal difficult. An alternative approach is to search for γ-rays from Andromeda beyond its galactic disk (67). Robust evidence for a significant extended excess is found. This emission appears to be distinct from the foreground with an extension upward of 120 to 200 kpc and a spectrum that peaks in the energy range of 3 to 20 GeV. Interestingly, this excess is consistent with the GC excess DM interpretation; however, confirming it and settling its origin is challenging. The line of sight toward Andromeda includes, in addition to its DM halo, the Milky Way DM halo and possibly a local DM filament joining them. Whether these additional components contribute to the observed γ-ray emission and/or are absorbed into the Milky Way foreground is not clear. Partitioning of the signal between them, along with their interplay with the foreground, is difficult to unravel. Because of the extension of the signal, modeling the bright foreground of the Milky Way is the greatest challenge in performing this analysis and interpreting the results.

In addition to γ-rays, measurements of charged CRs are exploited to search for DM annihilations, although this process is less straightforward as CRs change directionality and experience energy losses while propagating through the Galaxy. Because of the uncertainties in modeling the propagation of CRs in the Galaxy, inferring their origin is more challenging compared with the prospects for γ-rays. Antiparticles in CRs are better probes of DM because they are produced in amounts equal to those of their partners in DM-related processes (except for models of asymmetric DM; see 68), but they are far less common in CRs from other astrophysical processes. Positrons, antiprotons, and antinuclei are all promising messengers for DM interactions. In nonexotic processes, antiparticles in CRs are largely produced as secondary particles in the interaction of primary CRs (mainly protons) with the interstellar medium. The potential of DM searches with CRs is large (69–71) but is hindered by uncertainties in the CR propagation model and, for antiprotons, in the production cross section (69). In addition to constraints, analyses of the AMS-02 antiproton data have found that those data exceed predictions for secondary antiproton production in the energy range of a few GeV (72–74). The excess is observed if the DM contribution is fitted concurrently with the CR propagation parameters,[6] and it can be explained as DM annihilating into bottom quarks, with a mass and annihilation cross section compatible with those of the GC excess. Nevertheless, additional assessments of the uncertainties indicate that the antiproton data are compatible with secondary production (76). CR data, and antiprotons in particular, are therefore not sufficient to confirm a DM detection or to confirm the DM nature of the GC excess. They do, however, motivate further investigations.

[6]It is also assumed that the boron-to-carbon ratio in CRs, which is typically used in propagation models to constrain the diffusion coefficient, is not representative of the propagation for protons and antiprotons, as argued in Reference 75.

4.2. Other Interpretations

The GC excess has been found to be compatible with the combined emission of a population of unresolved pulsars, the leading competitor to the DM interpretation. The evidence for this interpretation is discussed in this section. CR outbursts also have been proposed as an explanation of the GC excess, although the evidence is not as compelling.

4.2.1. Pulsars. A morphology that follows the square of an NFW distribution, which is compatible with the GC excess, is not uniquely representative of a DM annihilation signal, at least for the GC region. It also traces the density profile of low-mass X-ray binaries (LMXBs) observed in the inner few hundred parsecs of the Andromeda galaxy (7). These sources are precursors to MSPs, and their spatial distribution is a proxy for the distribution of MSPs. These sources have γ-ray spectra that peak in the energy range of a few GeV and cut off at around 10 GeV. These observations are compatible, within uncertainties, with the measurement of the GC excess spectrum and morphology (7, 77–79). The GC excess could in fact originate from a large number of MSPs that are not individually resolved by *Fermi*–LAT, and their cumulative emission would manifest as a distinct extended component of the γ-ray sky. An MSP interpretation of the GC excess is very compelling and, it has been argued, is the leading one, although it faces some outstanding challenges, as discussed below and in Section 4.3.

An MSP spectrum is, within uncertainties, compatible with the spectrum of the GC excess, as shown in **Figure 5** (11). However, it differs from the DM annihilation spectrum that explains the excess. As an illustration, a comparison is shown in **Figure 5**: The DM annihilation spectrum falls more steeply below the GC excess peak energy compared with the spectrum of MSPs. Also,

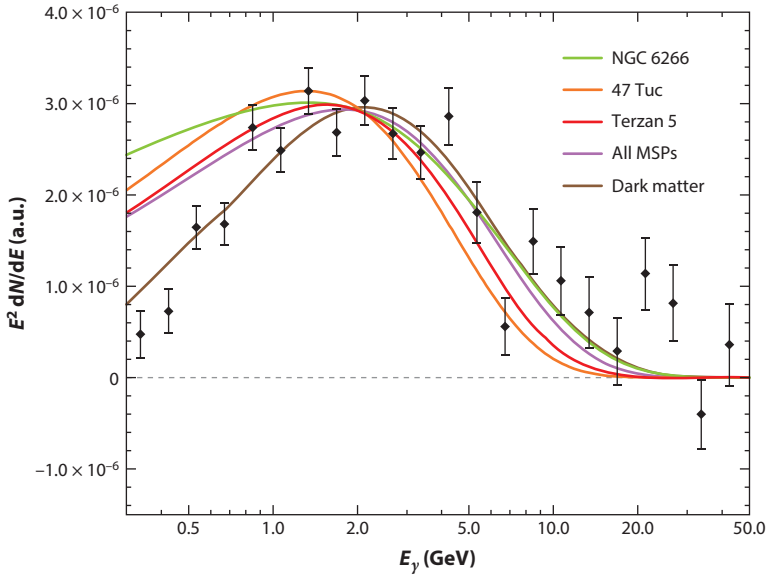

Figure 5

GC excess spectrum from Reference 11 overlaid with the γ-ray spectrum of MSPs detected by *Fermi*–LAT and with the spectrum of globular clusters (NGC 6266, 47 Tuc, and Terzan 5). The spectrum for DM annihilations into bottom quarks for a 43-GeV DM particle is also included. Abbreviations: DM, dark matter; GC, Galactic center; MSP, millisecond pulsar. Figure adapted with permission from Reference 11.

a typical pulsar spectrum turns off above ∼10 GeV, and if the high-energy tail in the GC excess spectrum is confirmed, a pulsar hypothesis is disfavored (see also 26). At the end of Section 2.1, I have noted the possibility that the spectrum of the GC excess could become harder at larger distances from the GC (17). If confirmed, this observation could not be explained by annihilating DM, at least in simpler scenarios in which there is one type of DM particle and for prompt γ-ray emission. In a model based on MSPs, this evolution can be explained by an additional contribution from inverse Compton scattering of the MSP high-energy electrons. Exploiting spectral differences to discriminate between a DM and MSP origin of the GC excess is, however, challenging at present given the large uncertainties in the measurement of the GC excess spectrum.

Some features of the GC excess, such as its high-latitude extension (up to at least 10°), were not predicted for MSPs. Nevertheless, it is possible that a population of MSPs extends to these latitudes as the relic of ancient globular clusters (80). These are dense star clusters that might have populated the Galactic halo in the past and have since been disrupted, leaving the MSPs behind. This is a plausible scenario, but there is currently no direct observational evidence for this relic other than potentially the GC excess, although radio surveys might be able to detect the MSPs directly, strengthening this interpretation. In addition to MSPs, young pulsars may contribute to the GC excess, although their contribution is limited to regions near the GC plane (81, 82). An MSP formation scenario that includes an admixture of primordial and dynamically formed precursor binaries is found compatible with the observation for some analyses of the GC excess (28). In addition to the spatial distribution, the luminosity function of an unresolved population of MSPs is also difficult to predict a priori, but a wide range of possibilities compatible with observations can explain the GC excess. Methodologies that attempt to extract this information from the data are discussed in Section 4.3 (see also 83).

The MSP interpretation of the GC excess has also been challenged (e.g., 84–86). It has been argued that because this interpretation employs observations of LMXBs in globular clusters and the inner Galaxy as well as γ-ray observations of globular clusters, the predicted number of MSPs populating the GC region (and their corresponding γ-ray flux) is too small to fully account for the GC excess (85). However, uncertainties affect these estimates because they are derived by extrapolating properties of a population of MSPs that evolved in an environment that is different from the Galactic bulge, where several MSPs would have to reside to explain the GC excess.

Ideally, an accurate a priori prediction for the γ-ray emission from an unresolved population of MSPs in agreement with the measurement of the GC excess would significantly strengthen this interpretation. Despite some of the challenges, a pulsar explanation of the GC excess remains compelling, and generally more accepted, compared with more exotic explanations such as DM. Additional evidence for and challenges to this hypothesis from statistical tools are discussed in Section 4.3.

4.2.2. Cosmic ray outbursts. Transient scenarios with CR outbursts at the GC (e.g., 87–89) have also been proposed as an explanation for the GC excess. CR protons or electrons injected by past activity of the central black hole Sgr A*, or nuclear starburst events, interact with the surrounding environment and generate γ-rays via π^0 production (for CR protons) or inverse Compton (for CR electrons). Evidence of an active past for the central region of the Galaxy, with the Fermi bubbles possibly being the most striking evidence, supports this hypothesis. CR proton outbursts would yield γ-rays correlated with the Galactic plane, tracing the gas, and therefore depart from the spherical morphology of the GC excess. CR electron outbursts are more compatible with the GC excess because of the smoother and approximately spherically symmetric γ-ray emission predicted in this scenario. These interpretations, however, arguably require a large degree of fine-tuning to describe the GC excess, and they fail in reproducing all aspects of it (89).

Finally, a steady-state CR diffusion scenario with a more realistic distribution of CR sources in the GC region than assumed has been proposed to explain the GC excess, as discussed in Section 3.2.1.

4.3. Statistical Tools

Significant progress in the interpretation of the GC excess has been possible based on methodologies that focus on the spatial morphology of the excess to determine whether it originates from an unresolved population of point sources (pulsars, but other classes of sources could also contribute) or from the smooth emission we expect from DM emission toward the GC. These techniques are based on a non-Poissonian photon statistics template (NPTF) analysis (90, 91) or on wavelet decomposition (92). The results based on these techniques find evidence of power at small angular scales in the *Fermi*–LAT data that could explain the entirety of the GC excess, and they make a compelling case for an unresolved point source population, such as MSPs, as the source of the excess rather than DM.[7] However, some challenges in the interpretation of these results remain. The results based on these techniques and their performance are outlined in this section.

4.3.1. Non-Poissonian photon statistics template. NPTF is a statistical tool incorporating templates for extended components that allow for statistical fluctuations on a pixel-by-pixel basis that deviate from Poissonian statistics. This type of template is employed to model an extended source that originates from a collection of discrete emitters (rather than from a smooth underlying distribution). The technique uses Bayesian methods to determine posterior distributions for the model parameters (including intensities of the model components) via a fit to the data, and it infers the source count distribution $\mathrm{d}N/\mathrm{d}F$ (the number of sources that contribute in the flux range F to $F + \mathrm{d}F$) for the unresolved population of sources it detects. The results of this technique applied to the *Fermi*–LAT inner Galaxy data are summarized in **Figure 6** (91). These results are based on a fit of the *Fermi*–LAT data employing point source templates that allow for non-Poissonian fluctuations with different spatial morphologies, a smooth DM annihilation template, the IEM, and the Fermi bubbles (note that the posterior probabilities for the IEM and Fermi bubbles templates are not shown in **Figure 6**). **Figure 6*b*** displays the posterior probability for the flux fraction for the point source components as well as for the NFW DM component obtained from the fit. These results show that the NFW point source template is favored by the data over other possibilities for a point source contribution and over a smooth DM contribution. The inferred source count distribution for the point source components, modeled as a broken power law function, is shown in **Figure 6*a***. On the basis of these results, the GC excess can be fully accounted for by a population of $\mathcal{O}(100)$ point sources accumulating at a flux below but very close to the *Fermi*–LAT sensitivity threshold.

Although there is strong evidence for a component in the data that is due to unresolved point sources, it is difficult to disentangle it from a potential DM signal. Simulations indicate that if an unresolved point source component is present in the data along with a DM signal, the NPTF technique can misattribute the DM signal to the unresolved point source component even for a bright DM signal (up to a luminosity a few times that of the GC excess) and for a spatial morphology of the unresolved component that is significantly different from that of the DM, as shown in Reference 95. In this proof of principle, the unresolved point source component is modeled with

[7] Although DM substructures could contribute to the discrete emission, in standard scenarios they do not fully account for the observed point-like structure claimed by these results (93).

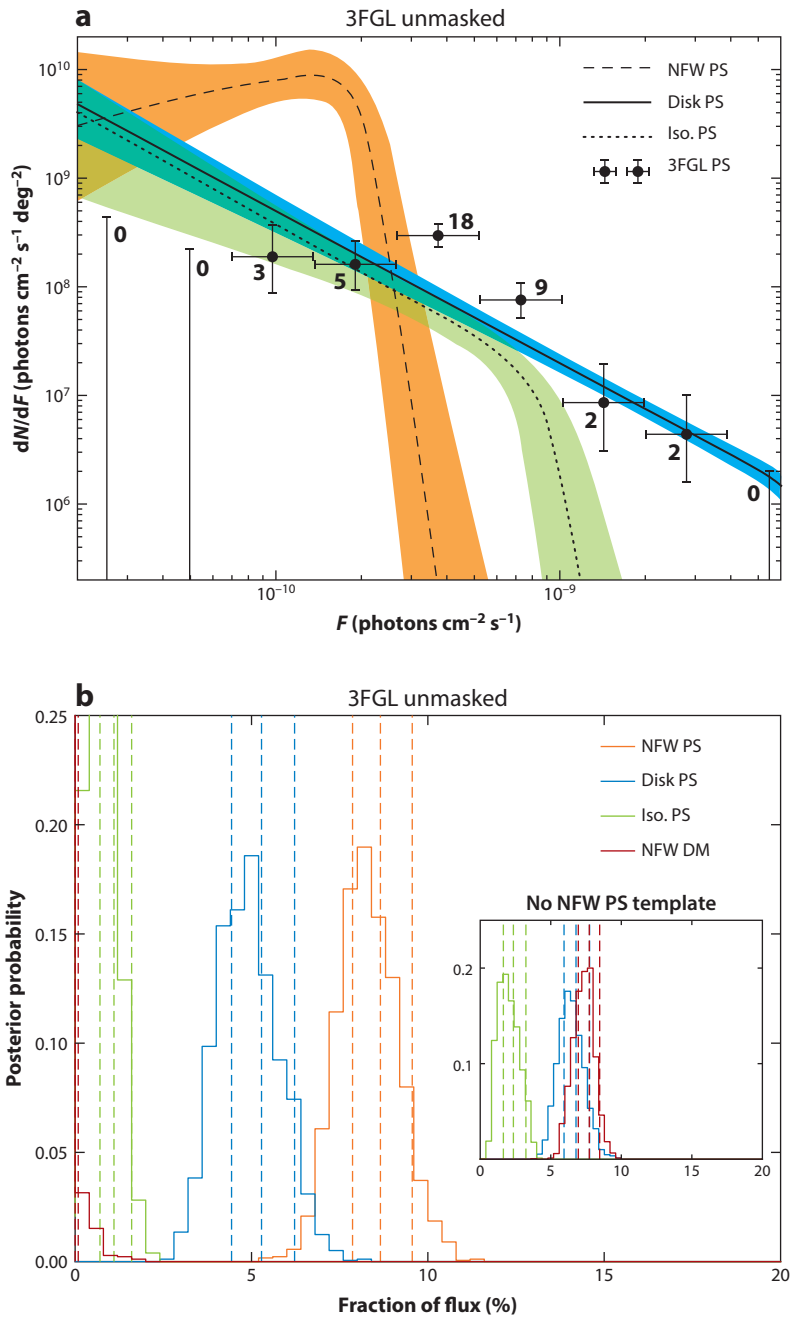

Figure 6

Results from application of the NPTF technique to the *Fermi*–LAT inner Galaxy data. (*a*) Inferred source count distribution for the PS-like components based on templates that allow for non-Poissonian fluctuations with different spatial morphologies, including isotropic (Iso. PS), disk-like (Disk PS), and DM annihilation (NFW PS, which is chosen to have a spatial morphology that is compatible with the GC excess—i.e., the square of the NFW density distribution with a slope $\gamma = 1.25$). Bold numbers indicate the observed sources in the 3FGL (94) in each bin. (*b*) Posterior probability for the flux fraction for selected model components, including smooth (NFW DM) and PS-like (NFW PS) contributions that follow a DM distribution, as well as PS-like isotropic (Iso. PS) and disk (Disk PS) distributions. Abbreviations: DM, dark matter; NFW, Navarro–Frenk–White; NPTF, non-Poissonian photon statistics template; PS, point source; 3FGL, *Fermi*–LAT third source catalog. Figure adapted with permission from Reference 91.

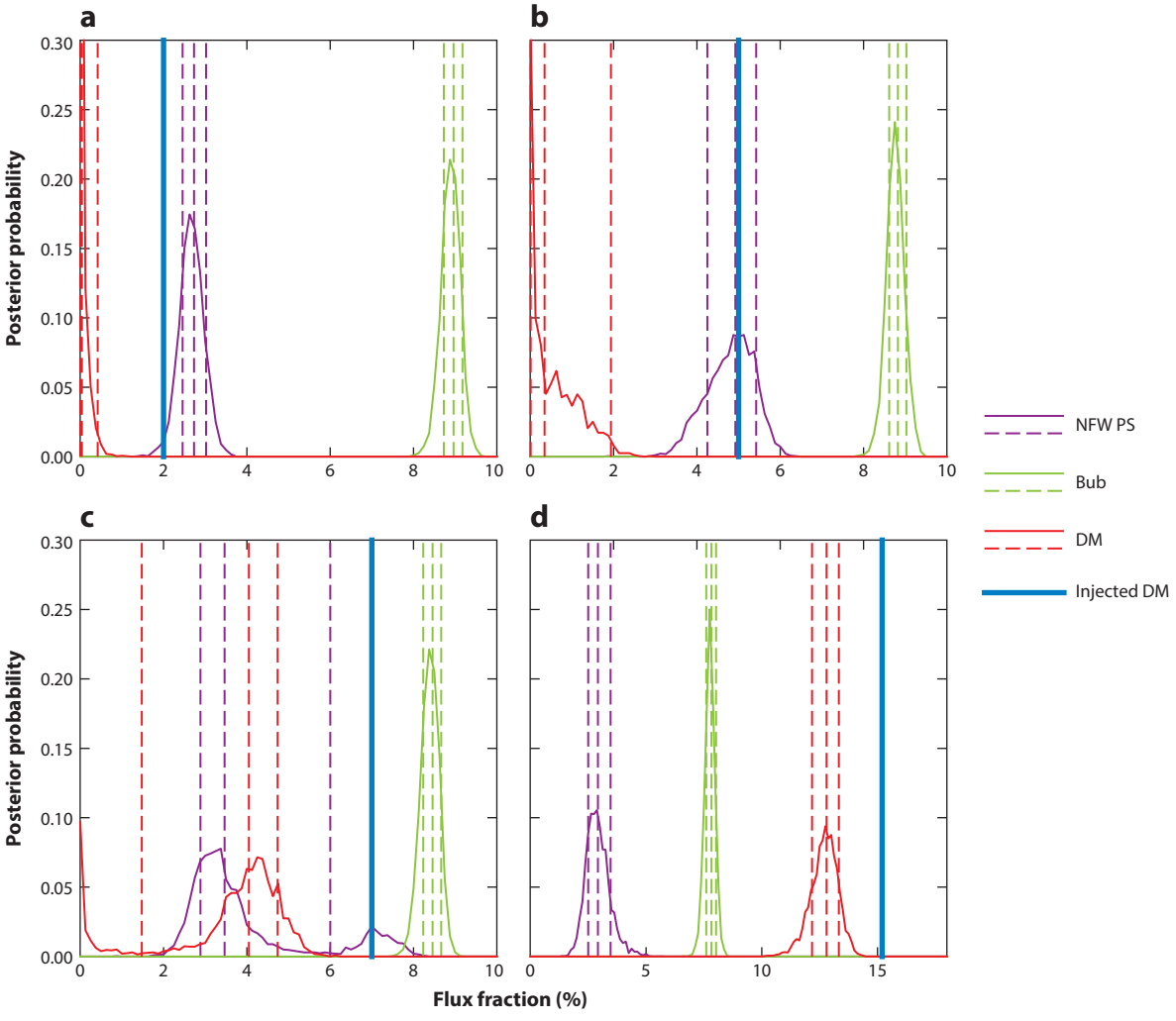

Figure 7

Results from Leane & Slatyer (95): posterior probability for the flux fraction for selected model components, including Fermi bubbles (Bub), smooth (DM), and PS-like (NFW PS) contributions. Each panel corresponds to a different level of DM signal injected in the simulation, indicated by the solid blue vertical line. Abbreviations: Bub, Fermi bubbles; DM, dark matter; NFW, Navarro–Frenk–White; PS, point source. Figure adapted with permission from Reference 95.

a spatial morphology that follows the Fermi bubbles (although it is not argued that the Fermi bubbles are expected to host such a population). The results are summarized in **Figure 7**, where the posterior probability for some of the templates used to fit the simulated data is shown. It can be seen that the correct amount of the injected DM signal is only detected for the largest flux fractions, while for the lower ones the smooth DM signal is at least partially concealed by the PS template. These conclusions are confirmed when injecting a simulated DM signal into the data, on top of any additional contributions that might already be there. This result demonstrates that if the data contain sufficient power at small angular scales and this component is not properly modeled, templates that capture the small-scale structure are favored by the fit even when they

do not match the underlying spatial morphology. Furthermore, uncertainties in modeling the Galactic γ-ray fore/background have a strong impact on the NPTF results: The non-Poissonian template used to model the unresolved source component—and, in particular, the fraction that originates from faint sources—strongly depends on the assumptions in the IEM that describes the fore/background emission, as shown in Reference 96. That study found that the reliability of the NPTF technique to distinguish an unresolved point source component from the fore/background decreases for small statistical fluctuations, causing these fluctuations to be misattributed to the fore/background emission even if they originate from faint point sources. The results from Reference 96 confirm that a significant fraction of the GC excess may originate from unresolved point sources (with a DM annihilation spatial morphology), but the uncertainty on this fraction due to modeling of the IE is large and up to the entirety of the GC excess. Therefore, it is not currently possible to precisely infer the fraction of the GC excess that can be ascribed to unresolved point sources with high confidence.

The difficulty of discriminating between the smooth and the point-like nature of the GC excess due to uncertainties in modeling of the IE is also apparent when examining the distribution of γ-ray counts per pixel in the observed residual γ-ray emission. The observed counts per pixel significantly exceed (by about an order of magnitude) the difference between the counts per pixel for a smooth DM annihilation signal and the counts per pixel for an unresolved point source contribution. Thus, uncertainties in the IEM, which cause the large residuals and therefore the large number of counts per pixel, might be so large as to hinder the ability to tease out the lower-level effects due the different interpretations of the GC excess (17).

To mitigate the impact of the IE model on the NPTF results, alternative models are considered in Reference 97, including the use of hydrodynamical simulations for the distribution of the interstellar gas (as discussed in Section 3.1.1 for References 18 and 28) and 3D modeling of the inverse Compton emission (35). In addition, a data-driven approach has been used by Buschmann et al. (97) to improve the IEM agreement with the γ-ray data at large angular scales using spherical harmonic decomposition of the IEM maps to capture large-scale mismodeling without affecting the small angular scale. Under these assumptions, the NPFT technique is reliable in extracting a DM signal from the data if one is present, in contrast to the results from Reference 95 in which different IEMs are employed. Also, Reference 97 concludes that the GC excess is still compatible with unresolved point sources rather than DM (although the possibility that DM contributes is not ruled out). It is also noted in Reference 97 that this work does not consider alternative spatial templates to model the GC excess (in addition to smooth or point-like). If the true unresolved point source or DM spatial distribution is different from those considered, the results might change in turn.

Because the spatial morphology of the GC excess cannot be reliably derived from the data (as discussed at length in this review; see Section 2.2 in particular), spatial templates to model it are judiciously chosen. Recent investigations of the GC excess with the NPTF technique have revealed that if the GC excess is not spatially symmetric (as is generally assumed) and the asymmetry is not properly modeled, then the results of the NPTF technique are not reliable (98, 99). Preliminary evidence also indicates that the GC excess might indeed present a north–south asymmetry (above and below the Galactic plane) and be smooth (rather than point-like) (98, 99). Furthermore, if the asymmetry is properly modeled, the evidence for an unresolved point source component in the data vanishes. Note that the evidence for the asymmetry is not conclusive because of the large modeling uncertainties (98, 99).

4.3.2. Wavelets. Wavelet decomposition techniques employ a convolution of the γ-ray data with a kernel function aimed at detecting γ-ray count fluctuations that are compatible with point

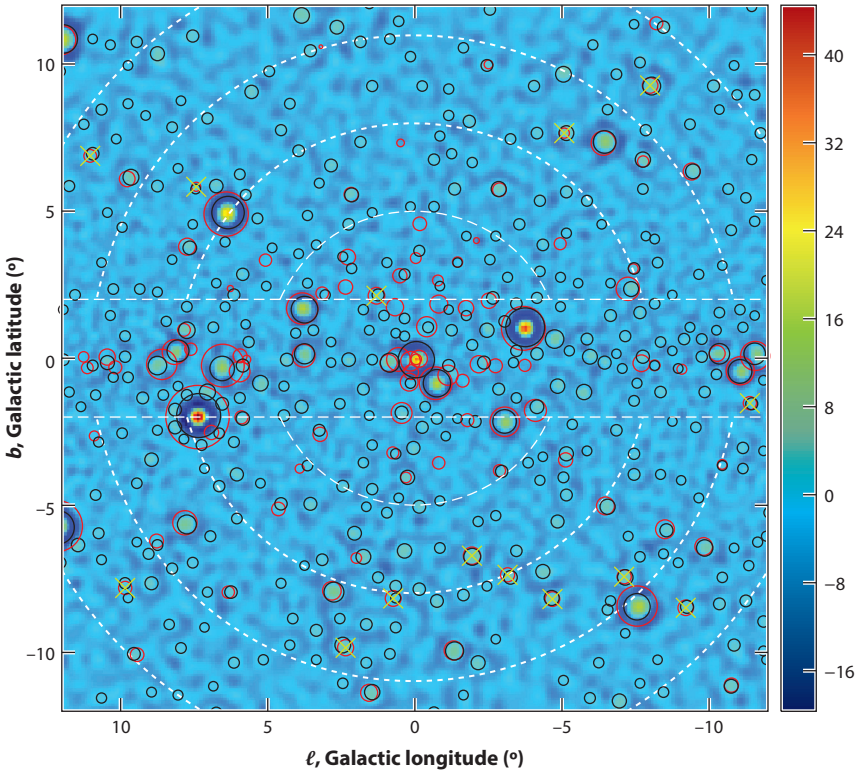

Figure 8

Results from Bartels et al. (92): signal-to-noise ratio of the wavelet transform for a 12° × 12° region about the Galactic center. Figure adapted with permission from Reference 92.

sources. This method detects small scale structure in the data and separates it from larger-scale contributions. The fore/background IE primarily contributes power at a larger scale and can be distinguished from an unresolved point source contribution using this method (92). While NPTF technique relies on assumptions in the IEM, analyses of the γ-ray data that employ wavelet decomposition are not as affected. Results from this technique are summarized in **Figure 8**: The signal-to-noise ratio of the wavelet transform, which can be interpreted as the local significance for a point source at that location, is shown for a 12° × 12° region about the GC. The statistics of the wavelet peaks is found to be compatible with a large number of faint point sources in the data, with a spatial distribution that is peaked toward the GC. For standard assumptions regarding the γ-ray luminosity of MSPs, this point source population can explain the full intensity of the GC excess.

It has, however, been argued that for latitudes higher than 5°, where the GC excess is significantly detected, there is not enough power at small angular scales to account for it, and the excess is diffuse in nature at these latitudes (100). Furthermore, when the *Fermi*–LAT fourth source catalog (4FGL) (101) is employed instead of the earlier versions, there is no evidence for sufficient power at small angular scales to explain the GC excess at lower latitudes as well (102), thus challenging the conclusions from Reference 92. It has been shown that the wavelet technique is very sensitive to the source catalog used to model the bright point sources in the region, and some of the point sources claimed in Reference 92 to contribute to the GC excess are indeed detected with high

statistical significance by *Fermi*–LAT in the 4FGL. Notably, the excess persists after accounting for the bright sources and regardless of the source catalog employed (102). Furthermore, by adopting constraints on the luminosity function compatible with data, this work shows that a large number of very faint point sources is required to fully account for the GC excess.

In summary for this section, in addition to the statistical techniques described above, the point-like or smooth nature of the GC excess has been tested with deep learning using convolutional neutral networks (CNNs) (103). Simulations indicate that CNNs are reliable in distinguishing between a point-like and smooth nature of the GC excess and also for the systematics that hinder the NPTF technique. When applied to the *Fermi*–LAT data, this work finds that the GC excess is consistent with the smooth emission predicted for a DM signal. These results are promising but warrant further investigation because of the reliance of the method on the IEM assumptions.

Testing the unresolved point source hypothesis is further complicated by uncertainties in modeling the IE component that is structured, and this complication in turn hinders attempts to distinguish between a point-like or smooth nature of the excess emission. As mentioned in Section 3, it is plausible that in addition to pulsars (and other Galactic γ-ray sources, such as SNRs), structure in the gas could contribute power at a small angular scale in the *Fermi*–LAT data. This possibility is shown in Reference 13, where it is observed that a large fraction of point sources detected toward and near the GC are spatially correlated with the gas-related γ-ray emission (from HI and H_2) closest to the GC and might be due to structure in the gas that is not correctly included in the model. Without supporting evidence—for example, a counterpart at other wavelengths—it is difficult to resolve the ambiguity. Therefore, it is plausible that unmodeled structure in the gas emission, including faint emission below the *Fermi*–LAT detection threshold, might also contribute to the unresolved source component observed in the data and, ultimately, might significantly confound the results discussed in this section.

5. FINAL REMARKS AND FUTURE PROSPECTS

The GeV excess remains a compelling indication of a new source of γ-rays—possibly DM. Because of the potential for discovery, the last decade's considerable effort aimed at identifying its nature is unsurprising. Substantial progress has been made in understanding and characterizing the signal, and modeling of the IE arguably represents the biggest challenge that must be addressed to resolve its origin. The determination of the GC excess relies on IEM assumptions, which vary across analyses and depend on the methodology used to constrain the IEM. Spectral and spatial properties of the GC excess vary based on the approach that is employed, and they are consistent, within uncertainties that are difficult to bracket, with different interpretations of the excess. The evolving interpretation of the GC excess over the years, outlined in this review, is rooted in the complex nature of the IEMs and is a symptom of the current modeling limitations and, in turn, of our limited ability to sufficiently constrain its properties. Although progress has been made to this end, significant uncertainties remain. None of the existing models provides a good description of the data (at the level of Poisson noise), with other excesses as well as deficits persisting in the data. Because of these complications, great caution should be taken in considering any of the current conclusions on the origin of the GC excess as final at this stage.

Looking forward, a γ-ray mission covering the energy range of *Fermi*–LAT but with significantly better angular resolution views of the GC region, and a correspondingly much improved ability to discriminate/identify the γ-ray emitters in the GC region, would allow us to more reliably tease out the excess emission and more precisely characterize its properties. This mission concept might unfold in the longer term; in the meantime, a combined effort that spans different observations and experiments has the biggest potential to unravel the nature of the GC excess.

Synergy with upcoming (and proposed) γ-ray experiments that complement *Fermi*–LAT observations down to MeV energies (AMEGO; see **https://asd.gsfc.nasa.gov/amego/index.html**) and up to TeV energies (with the Cherenkov Telescope Array; e.g., 104), including the *Fermi*–LAT energy range (GAMMA-400; see 105), would provide valuable data to further test interpretations of the GC excess and refine IE models. A conclusive resolution of the GC excess origin is, however, more likely to hinge on consistent detections that confirm it or rule it out. These scenarios include improvements of the dwarf spheroidal galaxy constraints following the discovery of many more dwarf galaxies by upcoming facilities, searches for the predicted MSP population to explain the excess by current and upcoming experiments, and measurements of CR antinuclei. Below, I discuss these items in turn.

If the GC excess is due to DM annihilations in the Galaxy, the most reliable confirmation is an independent detection, possibly from other DM indirect detection targets. Upcoming optical surveys (such as LSST) (106) are projected to observe several more dwarf spheroidal galaxies, significantly improving the reach for DM searches with γ-rays (depending on their J-factor) and, with it, prospects for settling the DM nature of the GC excess.

To confirm an MSP origin of the GC excess, these sources must be detected (in γ-rays and/or at other wavelengths). Whether these observations will have the final word on the interpretation of the GC excess hinges on how many MSPs are uncovered and on how well their properties can be constrained. While it stands to reason that there is an unresolved point source component in the data, and NPTF and wavelet techniques have shown that this component might be significant, these techniques currently do not reliably reconstruct its spectrum, luminosity function, and spatial morphology. This information is crucial in confirming an MSP interpretation of these results. Current and upcoming radio surveys have the potential to detect a large number (tens to hundreds) of bulge MSPs. A detection of this population, and the insight gathered regarding its properties, would help to identify this component in the γ-ray data and to more reliably determine its contribution to the GC excess (107).

Finally, a resolution of the nature of the GC excess could involve measurements of antinuclei in CRs with AMS-02 and GAPS (108). While antideuterons are very uncommon in CRs, DM annihilations might produce far more, surpassing by a large margin the predictions from other astrophysical sources. For example, the upcoming GAPS experiment (109) has a sensitivity in the energy range of a few GeV (for the nucleon spectrum), which is approximately two orders of magnitude above the astrophysical background (110) and, therefore, within the mass range of the GC DM signal and possibly the annihilation cross section.

SUMMARY POINTS

1. Since the first claim of its discovery, an incredible amount of work has been devoted to resolving the nature of the long-standing excess in the *Fermi*–LAT data toward the Galactic center. Its characterization, however, is uncertain and is strongly dependent on the assumptions employed to model the interstellar emission from the Galaxy.
2. The interstellar emission is dominant in the signal region, and its uncertainties, which are difficult to bracket, represent the biggest challenge in settling the nature of the excess. Although progress has been made to address the shortcomings of models for the interstellar emission, significant issues remain that affect all analyses of the Galactic center excess. However, prospects to address these issues and ultimately shed light on the nature of the Galactic center excess are limited because of the complexity of the Galaxy.

3. Dark matter annihilation is a viable explanation for the excess. An independent detection of a dark matter signal that is compatible with the interpretation of the Galactic center excess is imperative to confirm a dark matter origin.
4. Other interpretations for this excess have been proposed. The leading one is the combined emission of a collection of millisecond pulsars. While the evidence is very compelling, a detection of these sources in the inner region of the Galaxy is necessary to confirm it. Prospects for such confirmation rely on current and upcoming surveys that might detect these sources in large enough numbers.
5. The next few years promise additional insight into the nature of the Galactic center excess and, hopefully, will bring it to a resolution.

DISCLOSURE STATEMENT

The author is not aware of any affiliations, memberships, funding, or financial holdings that might be perceived as affecting the objectivity of this review.

ACKNOWLEDGMENTS

The author thanks Chris Karwin, Michael Peskin, Troy Porter, and Mauro Valli for a careful reading of this review and for the many insightful comments and suggestions. The author also thanks Ilias Cholis, Chris Karwin, Ryan Keeley, Oscar Macias, Nick Rodd, and Tracy Slatyer for providing the data included in the original figures and for the input and helpful discussions. The opinions expressed in this review are the author's, but insights were often born and developed from discussions with many in the community and over the years. For this, the author is especially grateful to Kevork Abazajian, Prateek Agrawal, Richard Bartels, Gianfranco Bertone, Anja Butter, Francesca Calore, Ilias Cholis, Greg Dobler, Rouven Essig, Doug Finkbeiner, Patrick Fox, Lisa Goodenough, Roni Harnik, Dan Hooper, Shunsaku Horiouchi, Manoj Kaplinghat, Chris Karwin, Savvas Koushiappas, Graham Kribs, Rebecca Leane, Tim Linden, Mariangela Lisanti, Sam McDermott, Igor Moskalenko, Tilman Plehn, Troy Porter, Nick Rodd, Ben Safdi, Tracy Slatyer, Emma Storm, Louis Strigari, Tim Tait, Flip Tanedo, Neal Weiner, and Christoph Weniger.

LITERATURE CITED

1. Bertone G, Hooper D, Silk J. *Phys. Rep.* 405:279 (2005)
2. Bertone G, Tait TMP. *Nature* 562:51 (2018)
3. Feng JL. *Annu. Rev. Astron. Astrophys.* 48:495 (2010)
4. Goodenough L, Hooper D. arXiv:0910.2998 [hep-ph] (2009)
5. Hooper D, Goodenough L. *Phys. Lett. B* 697:412 (2011)
6. Hooper D, Linden T. *Phys. Rev. D* 84:123005 (2011)
7. Abazajian KN, Kaplinghat M. *Phys. Rev. D* 86:083511 (2012)
8. Hooper D, Slatyer TR. *Phys. Dark Univ.* 2:118 (2013)
9. Gordon C, Macias O. *Phys. Rev. D* 88:083521 (2013)
10. Abazajian KN, Canac N, Horiuchi S, Kaplinghat M. *Phys. Rev. D* 90:023526 (2014)
11. Daylan T, et al. *Phys. Dark Univ.* 12:1 (2016)
12. Calore F, Cholis I, Weniger C. *J. Cosmol. Astropart. Phys.* 1503:038 (2015)
13. Ajello M, et al. (*Fermi*–LAT Collab.) *Astrophys. J.* 819:44 (2016)

14. Hunter S, et al. *Astrophys. J.* 481:205 (1997)
15. Abdo A, et al. (*Fermi*–LAT Collab.) *Phys. Rev. Lett.* 103:251101 (2009)
16. Abazajian KN, et al. *J. Cosmol. Astropart. Phys.* 1507:013 (2015)
17. Horiuchi S, Kaplinghat M, Kwa A. *J. Cosmol. Astropart. Phys.* 1611:053 (2016)
18. Macias O, et al. *Nat. Astron.* 2:387 (2018)
19. Boyarsky A, Malyshev D, Ruchayskiy O. *Phys. Lett. B* 705:165 (2011)
20. Su M, Slatyer TR, Finkbeiner DP. *Astrophys. J.* 724:1044 (2010)
21. Calore F, Cholis I, McCabe C, Weniger C. *Phys. Rev. D* 91:063003 (2015)
22. Carlson E, Linden T, Profumo S. *Phys. Rev. D* 94:063504 (2016)
23. Navarro JF, Frenk CS, White SDM. *Astrophys. J.* 490:493 (1997)
24. Karukes EV, et al. *J. Cosmol. Astropart. Phys.* 1909:046 (2019)
25. Gnedin OY, Kravtsov AV, Klypin AA, Nagai D. *Astrophys. J.* 616:16 (2004)
26. Linden T, Rodd NL, Safdi BR, Slatyer TR. *Phys. Rev. D* 94:103013 (2016)
27. Karwin C, et al. *Phys. Rev. D* 95:103005 (2017)
28. Macias O, et al. *J. Cosmol. Astropart. Phys.* 1909:042 (2019)
29. Bartels R, Storm E, Weniger C, Calore F. *Nat. Astron.* 2:819 (2018)
30. Helder EA, et al. *Space Sci. Rev.* 173:369 (2012)
31. Acero F, et al. (*Fermi*–LAT Collab.) *Astrophys. J. Suppl.* 223:26 (2016)
32. Ackermann M, et al. (*Fermi*–LAT Collab.) *Astrophys. J.* 750:3 (2012)
33. Gaggero D, et al. *J. Cosmol. Astropart. Phys.* 1512:056 (2015)
34. Carlson E, Linden T, Profumo S. *Phys. Rev. Lett.* 117:111101 (2016)
35. Porter TA, Johannesson G, Moskalenko IV. *Astrophys. J.* 846:67 (2017)
36. Jannesson G, Porter TA, Moskalenko IV. *Astrophys. J.* 856:45 (2018)
37. Ackermann M, et al. (*Fermi*–LAT Collab.) *Astrophys. J.* 840:43 (2017)
38. Porter TA, Johannesson G, Moskalenko IV. *Astrophys. J.* 887:250 (2019)
39. Kuhlen M, et al. *Astrophys. J.* 765:10 (2013)
40. Agrawal P, Batell B, Fox PJ, Harnik R. *J. Cosmol. Astropart. Phys.* 1505:011 (2015)
41. Cirelli M, Serpico PD, Zaharijas G. *J. Cosmol. Astropart. Phys.* 11:035 (2013)
42. Cirelli M, et al. *J. Cosmol. Astropart. Phys.* 1412:045 (2014)
43. Bertone G, Kong K, Ruiz de Austri R, Trotta R. *Phys. Rev. D* 83:036008 (2011)
44. Achterberg A, et al. *J. Cosmol. Astropart. Phys.* 1508:006 (2015)
45. Butter A, Murgia S, Plehn T, Tait TMP. *Phys. Rev. D* 96:035036 (2017)
46. Berlin A, Hooper D, McDermott SD. *Phys. Rev. D* 89:115022 (2014)
47. Carena M, Osborne J, Shah NR, Wagner CEM. *Phys. Rev. D* 100:055002 (2019)
48. Aalbers J, et al. (DARWIN Collab.) *J. Cosmol. Astropart. Phys.* 1611:017 (2016)
49. Slatyer TR. arXiv:1710.05137 [hep-ph] (2017)
50. Porter TA, Johnson RP, Graham PW. *Annu. Rev. Astron. Astrophys.* 49:155 (2011)
51. Conrad J, Reimer O. *Nat. Phys.* 13:224 (2017)
52. Strigari LE. *Rep. Prog. Phys.* 81:056901 (2018)
53. Geringer-Sameth A, et al. *Phys. Rev. Lett.* 115:081101 (2015)
54. Albert A, et al. (*Fermi*–LAT/DES Collab.) *Astrophys. J.* 834:110 (2017)
55. Abazajian KN, Keeley RE. *Phys. Rev. D* 93:083514 (2016)
56. Steigman G, Dasgupta B, Beacom JF. *Phys. Rev. D* 86:023506 (2012)
57. Hayashi K, et al. *Mon. Not. R. Astron. Soc.* 461:2914 (2016)
58. Klop N, Zandanel F, Hayashi K, Ando S. *Phys. Rev. D* 95:123012 (2017)
59. Ando S, et al. arXiv:2002.11956 [astro-ph.CO] (2020)
60. Benito M, et al. *J. Cosmol. Astropart. Phys.* 1702:007 (2017). Erratum. *J. Cosmol. Astropart. Phys.*1806:E01 (2018)
61. Bonnivard, et al. *Mon. Not. R. Astron. Soc.* 453:849 (2015)
62. Lisanti M, Mishra-Sharma S, Rodd NL, Safdi BR. *Phys. Rev. Lett.* 120:101101 (2018)
63. Pshirkov M, Postnov K, Vasiliev V. *Proc. Sci.* ICRC2015:867 (2016)
64. Ackermann M, et al. (*Fermi*–LAT Collab.) *Astrophys. J.* 836:208 (2017)

65. Eckner C, et al. *Astrophys. J.* 862:79 (2018)
66. McDaniel A, Jeltema T, Profumo S. *Phys. Rev. D* 97:103021 (2018)
67. Karwin C, Murgia S, Campbell S, Moskalenko I. *Astrophys. J.* 880:95 (2019)
68. Zurek KM. *Phys. Rep.* 537:91 (2014)
69. Giesen G, et al. *J. Cosmol. Astropart. Phys.* 1509:023 (2015)
70. Reinert A, Winkler MW. *J. Cosmol. Astropart. Phys.* 1801:055 (2018)
71. Gaggero D, Valli M. *Adv. High Energy Phys.* 2018:3010514 (2018)
72. Cuoco A, Heisig J, Korsmeier M, Krer M. *J. Cosmol. Astropart. Phys.* 1710:053 (2017)
73. Cholis I, Linden T, Hooper D. *Phys. Rev. D* 99:103026 (2019)
74. Cuoco A, Krer M, Korsmeier M. *Phys. Rev. Lett.* 118:191102 (2017)
75. Jannesson G, et al. *Astrophys. J.* 824:16 (2016)
76. Boudaud M, et al. *Phys. Rev. Res.* 2:023022 (2020)
77. Yuan Q, Zhang B. *J. High Energy Astrophys.* 3–4:1 (2014)
78. Abazajian KM. *J. Cosmol. Astropart. Phys.* 1103:010 (2011)
79. Petrović J, Serpico PD, Zaharijas G. *J. Cosmol. Astropart. Phys.* 1502:023 (2015)
80. Brandt TD, Kocsis B. *Astrophys. J.* 812:15 (2015)
81. O'Leary RM, Kistler MD, Kerr M, Dexter J. arXiv:1504.02477 [astro-ph.HE] (2015)
82. O'Leary RM, Kistler MD, Kerr M, Dexter J. arXiv:1601.05797 [astro-ph.HE] (2016)
83. Bartels RT, Edwards TDP, Weniger C. *Mon. Not. R. Astron. Soc.* 481:3966 (2018)
84. Hooper D, Linden T. *J. Cosmol. Astropart. Phys.* 1608:018 (2016)
85. Haggard D, Heinke C, Hooper D, Linden T. *J. Cosmol. Astropart. Phys.* 1705:056 (2017)
86. Linden T. *Phys. Rev. D* 93:063003 (2016)
87. Carlson E, Profumo S. *Phys. Rev. D* 90:023015 (2014)
88. Petrović J, Serpico PD, Zaharijaš G. *J. Cosmol. Astropart. Phys.* 1410:052 (2014)
89. Cholis I, et al. *J. Cosmol. Astropart. Phys.* 1512:005 (2015)
90. Lee SK, Lisanti M, Safdi BR. *J. Cosmol. Astropart. Phys.* 1505:056 (2015)
91. Lee SK, et al. *Phys. Rev. Lett.* 116:051103 (2016)
92. Bartels R, Krishnamurthy S, Weniger C. *Phys. Rev. Lett.* 116:051102 (2016)
93. Clark HA, Scott P, Trotta R, Lewis GF. *J. Cosmol. Astropart. Phys.* 1807:060 (2018)
94. Acero F, et al. (*Fermi*–LAT Collab.) *Astrophys. J. Suppl.* 218:23 (2015)
95. Leane RK, Slatyer TR. *Phys. Rev. Lett.* 123:241101 (2019)
96. Chang LJ, et al. *Phys. Rev. D* 101:023014 (2020)
97. Buschmann M, et al. arXiv:2002.12373 [astro-ph.HE] (2020)
98. Leane RK, Slatyer TR. arXiv:2002.12370 [astro-ph.HE] (2020)
99. Leane RK, Slatyer TR. arXiv:2002.12371 [astro-ph.HE] (2020)
100. Balaji B, Cholis I, Fox PJ, McDermott SD. *Phys. Rev. D* 98:043009 (2018)
101. Abdollahi S, et al. (*Fermi*–LAT Collab.) *Astrophys. J. Suppl.* 247:33 (2020)
102. Zhong YM, McDermott SD, Cholis I, Fox PJ. *Phys. Rev. Lett.* 124:231103 (2020)
103. List F, Rodd NL, Lewis GF, Bhat I. arXiv:2006.12504 [astro-ph.HE] (2020)
104. Doro M, et al. (CTA Consort.) *Astropart. Phys.* 43:189 (2013)
105. Galper AM, et al. arXiv:1412.4239 [physics.ins-det] (2014)
106. Ivezić Ž, et al. *Astrophys. J.* 873:111 (2019)
107. Calore F, et al. *Astrophys. J.* 827:143 (2016)
108. Cholis I, Linden T, Hooper D. arXiv:2001.08749 [astro-ph.HE] (2020)
109. Aramaki T, et al. (GAPS Collab.) *Astropart. Phys.* 59:12 (2014)
110. Aramaki T, et al. (GAPS Collab.) *Astropart. Phys.* 74:6 (2016)

Annual Review of Nuclear and Particle Science

Volume 70, 2020

Contents

Errata

An online log of corrections to *Annual Review of Nuclear and Particle Science* articles may be found at http://www.annualreviews.org/errata/nucl